BBA - General Subjects 1865 (2021) 129770

Contents lists available at ScienceDirect

BBA - General Subjects

journal homepage: www.elsevier.com/locate/bbagen

Modelling Förster resonance energy transfer (FRET) using anisotropy resolved multi-dimensional emission spectroscopy (ARMES)

Fiona Gordon, Saioa Elcoroaristizabal, Alan G. Ryder *

Nanoscale BioPhotonics Laboratory, School of Chemistry, National University of Ireland, Galway, Galway H91 CF50, Ireland

ARTICLE INFO

Keywords:
Fluorescence
Förster resonance energy transfer
Anisotropy
Protein
Chemometrics
Modelling

ABSTRACT

Background: Förster Resonance Energy Transfer (FRET) is widely used to study the structure and dynamics of biomolecular systems and also causes the non-linear fluorescence response observed in multi-fluorophore proteins. Accurate FRET analysis, in terms of measuring changes in donor and acceptor spectra and energy transfer efficiency is therefore critical.

Methods: We demonstrate a novel quantitative FRET analysis using anisotropy resolved multidimensional emission spectroscopy (ARMES) in a Human Serum Albumin (HSA) and 1,8-anilinonaphathalene sulfonate (ANS) model. ARMES combines 4D measurement of polarized excitation emission matrices (pEEM) with multivariate data analysis to spectrally resolve contributing fluorophores. Multivariate analysis (Parallel Factor, PARAFAC and restricted Tucker3) was used to resolve fluorophore contributions and for modelling the quenching of HSA emission and the HSA-ANS interactions.

Results: pEEM spectra were modelled using Tucker3 which accommodates non-linearities introduced by FRET and a priori chemical knowledge was used to optimise the solution, thus resolving three components: HSA emission, ANS emission from indirect FRET excitation, and ANS emission from direct excitation. Perpendicular emission measurements were more sensitive to indirectly excited acceptor emission. PARAFAC modelling of HSA, donor emission, separated ANS FRET interacting (Tryptophan) and non-interacting (Tyrosine) components. This enabled a new way of calculating quenching constants using the multi-dimensional emission of individual donor fluorophores.

Conclusions: FRET efficiency could be calculated using the multi-dimensional, resolved emission of the interacting donor fluorophores only which yielded higher ET efficiencies compared to conventional methods.

General significance: Shows the potential of multidimensional fluorescence measurements and data analysis for more accurate FRET modelling in proteins.

1. Introduction

Förster Resonance Energy Transfer (FRET) is the non-radiative energy transfer from a donor fluorophore to a nearby acceptor fluorophore (usually <10 nm) [1], is widely used to study biomolecular systems [2–4] often being referred to as a 'spectroscopic ruler' [5]. Molecular systems in which FRET occur can be studied via changes in spectroscopic properties such as fluorescence intensity, lifetime, quantum efficiency, and anisotropy [6,7]. Conventionally, parameters, such as FRET efficiency, are calculated using 2-D (wavelength vs. emission intensity) steady-state, or time-resolved, measurements of the quenching of donor fluorescence intensity, the enhancement in acceptor fluorescence intensity or the decrease in the donor lifetime [7,8]. However, the low information content of simple 2-D spectral measurements from complex spectra with overlapping emission from multiple fluorophores makes multi-dimensional fluorescence (MDF) measurements more suitable for resolving the spectra of constituent fluorophores.

Systems exhibiting FRET are inevitably multi-component systems

Abbreviations: ANS, 1, 8-anilinonaphathalene sulfonate; ARMES, anisotropy resolved multidimensional emission spectroscopy; EEM, excitation emission matrices; FRET, Förster resonance energy transfer; HH, horizontal-horizontal; HSA, Human Serum Albumin; HV, horizontal-vertical; IFE, inner filter effect; LOR, limit of reporting; MCR, multivariate curve resolution; MDF, multi-dimensional fluorescence; PARAFAC, parallel factor; pEEM, polarized EEM; pTSFS, polarized TSFS; Trp, tryptophan; TSFS, total synchronous fluorescent scans; Tyr, tyrosine; VV, vertical-vertical; VH, vertical-horizontal.

* Corresponding author.
E-mail addresses: F.GORDON2@nuigalway.ie (F. Gordon), elcoroaristizabal@nuigalway.ie (S. Elcoroaristizabal), alan.ryder@nuigalway.ie (A.G. Ryder).

https://doi.org/10.1016/j.bbagen.2020.129770
Received 5 August 2020; Received in revised form 9 October 2020; Accepted 19 October 2020
Available online 22 October 2020

consisting of, at minimum, a donor and an acceptor molecule (FRET pair) which may or may not be fluorescent. For a given FRET pair with a fluorescent donor and acceptor, three main spectral contributions often need to be resolved which correspond to : direct donor fluorescence, direct acceptor fluorescence, and FRET induced acceptor fluorescence (indirect donor fluorescence) [9]. All of these contributions can be spectrally overlapped and thus spectral unmixing methods are required [10,11]. MDF spectroscopy, such as Excitation Emission Matrices (EEM) and total synchronous fluorescent scans (TSFS) [12,13], combined with chemometric methods can resolve overlapped fluorescence signals. TSFS measurements have a major advantage in terms of reducing the effect of Rayleigh scatter at the blue edge of the emission where tyrosine (Tyr) emits [14]. MDF spectroscopy can be further enhanced by adding steady-state anisotropy (or polarization) information making a 4D measurement. The use of polarized EEM (pEEM) and polarized TSFS (pTSFS) measurements provide a new approach for studying complex systems containing proteins [15,16]. This measurement methodology has been further developed into anisotropy resolved multidimensional emission spectroscopy (ARMES) which combines multivariate data analysis methods like Parallel Factor (PARAFAC) or Multivariate Curve Resolution (MCR) to specifically resolve individual fluorophore contributions from complex spectra [17,18]. In ARMES, we analyse explicitly the anisotropic emission of proteins separately using the $EEM_{\parallel}$ (parallel) and $EEM_{\perp}$ (perpendicular) spectra with a view to identifying and analysing both intensity and profile changes.

PARAFAC is the most popular method for resolving MDF spectra [19,20], and here it is used for the analysis of donor (HSA) quenching. However, PARAFAC is not always suitable for analysing fluorescence data from systems which exhibit FRET. As PARAFAC is a trilinear model it requires that the fluorophores in a mixture are non-interacting and that the underlying fluorescent components have independent concentration, excitation, and emission profiles. However, in FRET, coupling between the donor excitation spectrum and acceptor emission spectrum generates non-linearity [21] in the fluorescence emission and thus more flexible methods like Tucker3 are required [22]. Tucker3 does not require trilinear data and thus any component in a certain mode can interact with any component in the other two modes [23]. Restricted Tucker3 models have successfully modelled FRET interactions [24–26] through the use of a priori chemical knowledge to constrain models to the expected interaction terms (i.e. indirect excitation component with the excitation profile of the donor and emission profile of the acceptor). However, most studies to date, have been limited to the analysis of unpolarized EEM data from small sized sample datasets with no chemical validation of the obtained chemometric solutions [24–26].

Here we aim to better model hetero-FRET processes in proteins using ARMES [17] by the use of restricted Tucker3 on a relatively large sized sample set. Fluorescence anisotropy and polarized emission based methods have been used for studying FRET processes in proteins [27,28], however, this has not been attempted using MDF measurements or chemometric data analysis. A human serum albumin (HSA) and 1,8-anilinonaphthelene (ANS) model system is used and was chosen for two reasons. First, HSA only has a single tryptophan (Trp) fluorophore, and second extensive data was available on a similar bovine serum albumin ANS model system [29,30]. HSA is heart shaped protein [31] composed of three domains (I, II, and III) (Fig. 1A) each of which comprises of two subdomains (A and B) [32]. The intrinsic fluorescence of HSA is dominated by the single tryptophan fluorophore (Trp-214) located between IA and IIB, with a smaller contribution from 17 tyrosine residues, whereas the contribution of Phenylalanine is negligible [7]. Tyrosine (Tyr) fluorophores are distributed throughout the protein and are generally more solvent exposed [33]. There are two primary small molecule binding sites, Sudlow I (located in subdomain IIA, in close proximity (~2 nm) to Trp-214 [34,36]) and Sudlow II (located in subdomain IIIA, further from Trp-214 > 2 nm), along with a number of secondary binding sites [36,37]. ANS (Fig. S1A/B, SI) is a commonly used fluorophore, known to bind with high affinity to HSA [38]. ANS (Fig. 1B) is weakly fluorescent when free in aqueous buffer, however, upon incorporation into the hydrophobic binding sites of HSA there is a significant increase in quantum yield (Fig. S1A/B, SI), along with an increase in the anisotropy and fluorescent lifetime values of the molecule [39–41]. When mixed, the HSA Trp-214 fluorophore acts as the FRET donor for the spectrally overlapped and hydrophobically bound ANS acceptor molecules. Many HSA-ligand interaction studies which use FRET tend to focus only on the analysis of intrinsic HSA emission quenching [42,43] and some of the information contained in the global emission of the system may go unused.

Here, we aim to first resolve, using multivariate data analysis, HSA-ANS emission into its three major components: indirectly excited (via hetero-FRET) ANS acceptor emission, and the directly excited acceptor and donor HSA emission. This resolving of the main emission components assists in the interpretation of complex MDF spectra from spectrally overlapped multi-fluorophore systems [21,44]. Secondly, we aim to resolve the donor, HSA, emission into its constituent Trp and Tyr emission to allow more accurate analysis of quenching effects, calculation of separate Stern-Volmer quenching constants, and FRET efficiency values.

2. Materials and methods

2.1. Sample preparation

Stock (3×10^{-5} M) solutions of Human Serum Albumin (HSA) (*Sigma*, cat. no. A1887, lot no. SLBM7779V) and 1,8-anilinonaphathelene sulphate (3×10^{-4} M) (*Sigma*, cat. no. 10419) were prepared in phosphate buffered saline (pH 7.4) in amber coloured volumetric flasks. Twenty samples with ANS/HSA molar fractions/labelling ratios from 0.05–10 were prepared in triplicate ($n = 60$). The HSA concentration was kept constant (1.5×10^{-5} M) while varying the ANS concentration (7.5×10^{-7}–1.5×10^{-4} M) in the buffer. Samples containing only HSA (1.5×10^{-5} M) and ANS (1.5×10^{-4} M) solutions were also prepared in

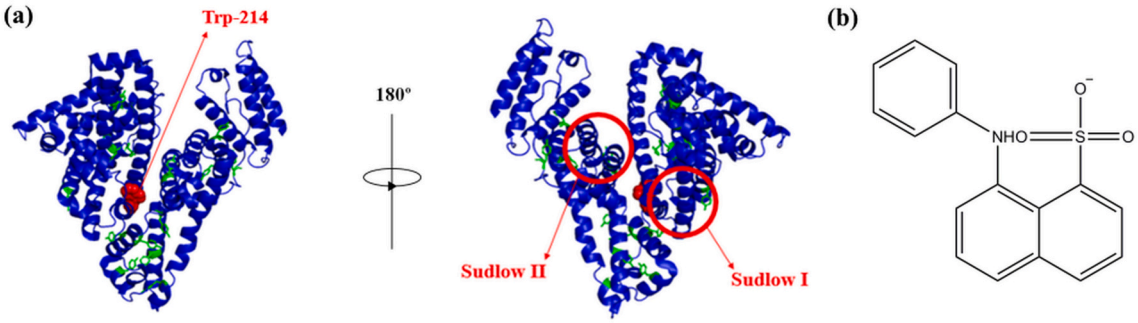

Fig. 1. (a) Human serum albumin with a single tryptophan residue (red) and 17 tyrosine residues (green) highlighted. The major binding sites (Sudlow I & II) are also indicated above. (Image sourced from PDB and edited using Pymol) (b) 1,8-anilinonapthalene sulfonate, the hydrophobic small molecule acceptor used.

triplicate by adding equal amounts of stock solution and buffer. All solutions were prepared at room temperature in a laminar flow hood and then stored at −70 °C. Prior to spectral analysis samples were defrosted overnight at ~4 °C and then pipetted into 4 × 10 mm pathlength quartz cuvettes (*Light-path Optical Ltd UK*).

2.2. Spectral measurements

UV–Vis absorption spectra were obtained using Cary 60 UV–Vis Spectrophotometer (*Agilent Technologies*) along the short axis of the cuvette (4 mm) at a scan rate of 1200 nm min^{-1} and a temperature of 25 °C. Steady-state pTSFS spectra were collected using a Cary Eclipse Spectrophotometer (*Agilent Technologies*), fitted with wire-grid polarizers to enable steady-state anisotropy measurements in the UV region [18], and a temperature-regulated multi-cell holder. pTSFS data was collected over an excitation range of λ_{ex} = 240–440 nm at varying wavelength offsets of 20–330 nm (λ_{em} = 260–570 nm) with 2 nm step increments for both axes. Samples were excited along the short axis (4 mm) and emission was collected along the long axis (10 mm). Excitation and emission monochromators slit widths were 10 nm, the scan rate was 1200 nm min^{-1} and the photomultiplier tube detector voltage was set to 555 V. All samples were measured using four different polarizer settings to generate four different TSFS spectra: $TSFS_{VV}$ (vertical-vertical), $TSFS_{VH}$ (vertical-horizontal), $TSFS_{HH}$ (horizontal-horizontal), $TSFS_{HV}$ (horizontal-vertical). The anisotropy (r) was calculated using the standard anisotropy formula (Eq. (1)) [7], which was then used to construct the corresponding multidimensional anisotropy maps. Steady state anisotropy follows the Perrin equation (Eq. (2)), where r_0 is the value of anisotropy at t = 0 after short pulse excitation, τ is the fluorescence lifetime of the fluorophore, η is the local viscosity of the solution, and V is the hydrodynamic radius.

$$r = \frac{I_{VV} - GI_{VH}}{I_{VV} + 2GI_{VH}} \text{ or } \frac{I_{\parallel} - GI_{\perp}}{I_{\parallel} + 2GI_{\perp}}, \text{where } G = \frac{I_{HV}}{I_{HH}} \quad (1)$$

$$r = \frac{r_0}{1 + \frac{\tau RT}{\eta V}} \quad (2)$$

2.3. Data pre-processing and analysis

All data analysis was conducted using the PLS toolbox ver. 8.2.1 (Eigenvector Research Inc.), MATLAB ver. 9.1.0 (The Mathworks Inc.) and in-house written codes. TSFS measurements were used in preference to EEM in order to minimize the Rayleigh scattering contamination when using wavelength offsets of Δλ ≥ 20 nm [14]. $TSFS_{HV}$ and $TSFS_{HH}$ measurements were used to calculate the G-factor ($G = I_{HV}/I_{HH}$) and this was used to correct the $TSFS_{VH}$ spectra for polarization bias, giving the corrected perpendicular $TSFS_{\perp}$ spectra. The $TSFS_{VV}$ spectra are referred as the parallel polarized, $TSFS_{\parallel}$, spectra. The total unpolarized $TSFS_T$ spectra were calculated from the pTSFS spectra as follows: $TSFS_T = TSFS_{\parallel} + 2 \times TSFS_{\perp}$, and were used to assess the advantages of using pTSFS measurements instead of conventional TSFS measurements (the $TSFS_T$ data is equivalent to a normal TSFS measurement made without polarizers). $TSFS_{\parallel}$ and $TSFS_{\perp}$ datasets, were then subjected to Raman scattering minimization and inner filter effect (IFE) correction [45]. Raman scattering was reduced by blank subtraction (PBS buffer spectrum) from the TSFS spectrum. IFE correction was necessary due to the change in the optical density of the samples (Abs = 0.21 ± 0.004 to 0.97 ± 0.01, at 280 nm, 4 mm pathlength) with increasing ANS concentration. The absorbance-based approach, was implemented as previously described [44], using the limit of reporting (LOR) [45].

$TSFS_{\perp}$ and $TSFS_{\parallel}$ datasets were then transformed from a non-trilinear TSFS layout to a trilinear EEM layout for chemometric data analysis, and hereafter designated as t-EEM_T, t-$EEM_{\perp}$, and t-$EEM_{\parallel}$ [46]. Interpolation was applied in order to handle the area with no experimentally acquired spectral information in the t-EEM layout [14]. Second-order scatter was also corrected via interpolation [47]. t-EEM data were smoothed using the Savitzky-Golay algorithm in order to reduce unwanted noise. The pre-processed t-EEM_T, t-$EEM_{\perp}$, and t-$EEM_{\parallel}$ data were arranged into a three-way array ($\underline{\mathbf{X}}$) of size 63 × 131 × 101 (samples (excluding ANS stock) × λ_{em} × λ_{ex}) and normalized to unit norm (sample mode) in order to compensate for large intensity differences between samples when modelling. The sub-region of HSA donor emission (non-normalized) were cut to a three-way array ($\underline{\mathbf{X}}$) of size 63 × 51 × 31, before chemometric analysis.

2.4. Chemometric methods

2.4.1. MCR-ALS analysis of UV–Vis absorbance spectra

UV–Vis titration data were analysed by MCR-ALS [48] in order to determine the concentration profiles and spectra of ANS, HSA, and the complex formed during the binding process [49]. The data matrix **D** (66 × 41) was constructed with rows representing the UV–Vis spectra at the different molar fractions (20 ANS/HSA molar ratio solutions) and ANS and HSA stock solutions in triplicate, and in the columns (41) the absorbance values measured at each spectral wavelength between 240 and 440 nm (every 5 nm). MCR-ALS [50] entails decomposing the matrix **D** as: $\mathbf{D} = \mathbf{C}\cdot\mathbf{S}^T + \mathbf{E}$ by iterative alternating least-squares (ALS) optimization of **C** (matrix of the concentration profiles) and $\mathbf{S}^T$ (the spectra matrix) to minimize of the Frobenius norm of **E** (the residuals). To initialize the optimization process, a SIMPLISMA based algorithm was used. The data matrix was decomposed during ALS optimization implementing non-negativity constraints on both concentration and spectral profiles to ensure that the mathematical solution was chemically meaningful. Correspondence among species was used to restrict the rotational ambiguity, i.e. presence/absence of analytes in stock samples was actively set [51]. Singular Value Decomposition (SVD) was used to estimate the number of components and this was found to be three in all cases.

2.4.2. Multiway analysis of FRET

t-EEM data were analysed by PARAFAC [52–54] and Tucker 3 [22] depending on the structure of the data. PARAFAC is the most commonly used technique for modelling of EEM data as it usually provides unique solutions for complex multicomponent mixtures where the components are non-interacting [20,55]. If the EEM three-way array ($\underline{\mathbf{X}}$) of size I × J × K (samples × λ_{em} × λ_{ex}) is trilinear, it can be decomposed into a triad of matrices **A** (I × R), **B** (J × R), and **C** (K × R) and a residual tensor $\underline{\mathbf{E}}$ (I × J × K), representing the relative contribution ($\mathbf{a_r}$), the emission ($\mathbf{b_r}$), and excitation profiles ($\mathbf{c_r}$) of each fluorophore (R) in the samples (I). In PARAFAC, a core array tensor $\underline{\mathbf{G}}$ (R × R × R), containing ones on its super-diagonal and zeros elsewhere, eliminates the problem of rotational ambiguities faced by bilinear methods [56,57]. Thus, PARAFAC requires data of full rank, i.e. with the same number of components in each mode, or in other words, components of the data must be linearly independent and non-interacting [19]. However, the complex multidimensional emission of multi-fluorophore systems like proteins which undergo FRET [21], do not fulfil the conditions necessary to achieve reliable PARAFAC solutions because of proportionality rank deficiency in both the excitation and emission profiles between the donor-acceptor fluorophores. In spectroscopic terms, the acceptor emission arising from indirect excitation (i.e. via FRET) will have an excitation profile similar to the donor fluorophore rather than a unique excitation profile which results in a linearly dependent component.

In such cases where the trilinear requirement is not satisfied, the data can be modelled using Tucker3 [22,57] which preceded the development of PARAFAC, and PARAFAC can be considered as a constrained version of Tucker3 [58]. Tucker3 allows for extraction of different numbers of components in each of the three modes (i.e. does not require trilinear data) and any component in a certain mode can interact with any component in the other two modes [23]. In Tucker3 the t-EEM dataset, with dimensions I × J × K, is decomposed in a similar way to

PARAFAC into: three matrices **A** (I × R), **B** (J × S), and **C** (K × T), a residual tensor **E** (I × J × K), and one core array tensor **G** (R × S × T) (which can have interactions between any two modes). In this case, R is the number of components in the first mode, S is the number of components in the second mode, and T is the number of components in the third mode. So, the number of components can be different in the different concentration or spectral modes.

However, despite Tucker3's ability to cope with non-linear data, it has not gained significant attention due to the rotational freedom of the model which leads to multiple solutions from which it may be difficult to determine the correct result. In cases where PARAFAC is too restricted and Tucker3 is too flexible, restricted Tucker3 is a potential solution [24–26]. Restricted Tucker3 models minimize ambiguity in the solutions by using a priori chemical knowledge of the system. The tucker core (**G**) which allows for components in a certain mode to interact with any component in the other two modes, is replaced with a defined core array in which most elements are forced to zero, reducing the number of interaction terms, thus simplifying the model, and making the solutions easier to interpret. It is important to note, however, that all multivariate data analysis solutions in the case of multi-fluorophore proteins, are only a model of the observed changes, and these solutions are unlikely to be a completely accurate representation of the true photophysical processes. Both PARAFAC and Tucker3 fit spectral data using the excitation, emission, and scores (with independent components in all three modes in PARAFAC and linearly dependent components in the case of Tucker3). This assumes that the shape of the excitation and emission spectral profiles of components do not vary across the sample set being modelled. This is however, unlikely in the case of proteins where fluorophores like Trp are sensitive to the environment and display spectral changes on going from hydrophobic to hydrophilic environments [7]. Here, we used a combination of PARAFAC and Tucker 3 modelling to provide different insights into protein emission. PARAFAC for example was only used for the analysis of donor quenching as FRET induced emission was not included. The Tyr and Trp components of the donor emission behaved in a more tri-linear fashion facilitating PARAFAC resolution. Tucker 3 was applied to the more non-linear emission from the HSA-ANS interaction.

3. Results and discussion

3.1. Spectral analysis

The t-EEM spectra generated for HSA-ANS complexes have three emission peaks (Fig. 2): Peak A ($\lambda_{ex}/\lambda_{em}$ = 280/~350 nm) corresponding to intrinsic HSA emission (combination of Trp and Tyr emission), which is quenched and blue-shifted upon ANS addition. The strong emission blue-shift (~24 nm) up to ~2 M equivalents of ANS, correlates with increasing FRET as ~2 molecules of ANS become bound to each HSA molecule. Peaks B ($\lambda_{ex}/\lambda_{em}$ = 270/380 nm) and C ($\lambda_{ex}/\lambda_{em}$ = 270/470 nm) correspond to fluorescence of ANS located in the hydrophobic sites of HSA. For ANS peak B (λ_{em} = ~470 nm), the intensity is expected to rise because of two factors: increasing concentration of bound ANS which is directly excited, and via indirectly excited ANS (via FRET energy transfer from Trp). From t-EEM spectral analysis it was observed that the ANS emission maximum (Fig. 2, peak (B & C)) was blue-shifted, as expected, relative to ANS in aqueous buffer, upon incorporation into the hydrophobic binding sites (Fig. S1B, SI).

The calculated spectral overlap (Eq. (3)) between HSA emission and

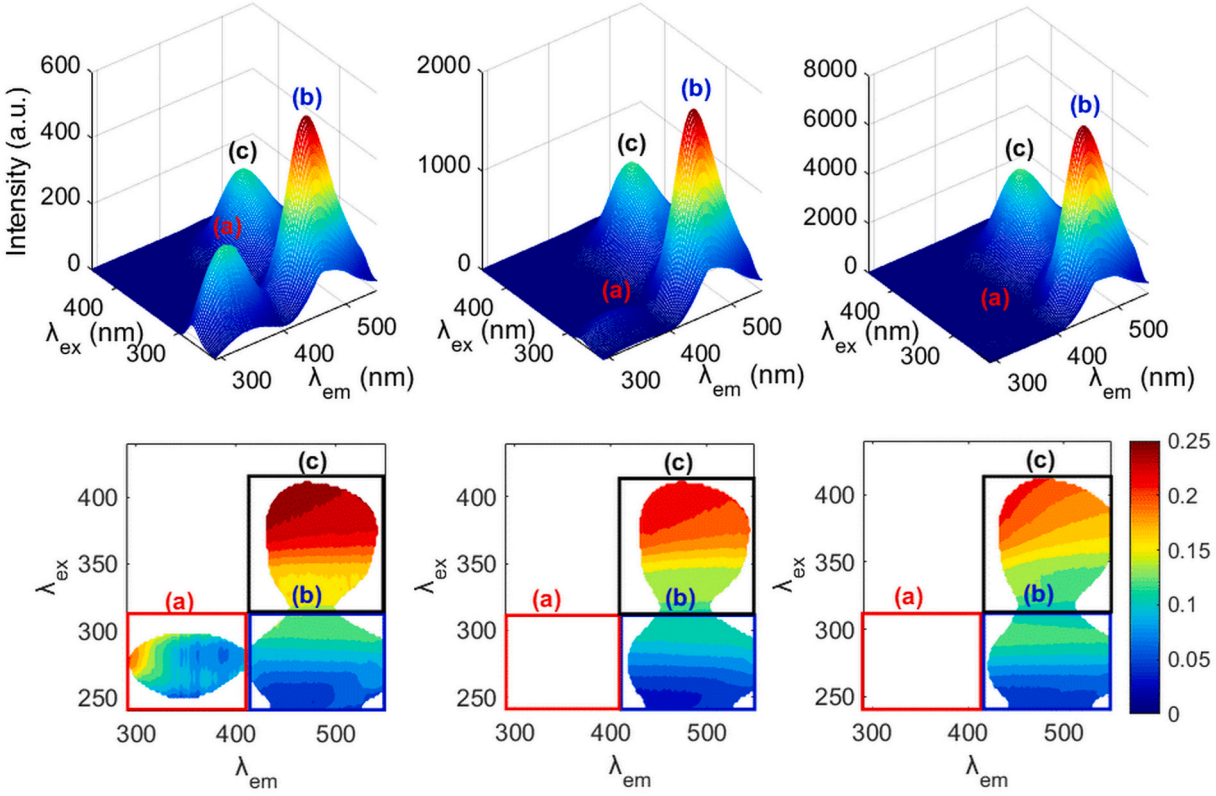

Fig. 2. (Top Row) t-EEM$_T$ spectra of representative HSA-ANS samples with varying [ANS]/[HSA] ratios: (left) 0.25, (middle) 1.0, and (right) 10. Three main emission bands are observed: (a) Intrinsic HSA fluorescence (composed of Tyr & Trp emission); (b) ANS fluorescence bound to HSA (composed of direct & indirectly excited emission); and (c) ANS fluorescence bound to HSA (direct emission only). (Bottom row) Corresponding *aniso*-t-EEMs maps for the same samples showing the large changes in anisotropy induced by FRET. Region a, corresponding to intrinsic HSA fluorescence shows depolarisation of emission due to intrinsic homo- and hetero-FRET (Tyr-Tyr/Tyr-Trp) within HSA. Region b, corresponding to ANS emission (indirect and direct emission) is depolarised due to hetero-FRET (Trp-ANS). Region c shows higher anisotropy due to ANS binding to the much larger HSA, upon addition of ANS variation is observed in this region.

ANS absorption spectra $J(\lambda) = 5.756 \times 10^{15}\ nm^4\ M^{-1}\ cm^{-1}$ (Fig. S1D, SI) was used to calculate an R_0 of 4.82 nm (Eq. (4)), assuming an orientation factor of $\kappa^2 = 0.666$ and using values of $\phi_D = 0.13$, $\eta = 1.33$ for the quantum efficiency of the donor and the refractive index of the sample, respectively. The obtained *r* values ($r = 6.4$–4.1 nm, for [ANS]/[HSA] = 0.25–10) fall within the range $0.5R_0 < r < 1.5R_0$ which implies FRET occurs as ANS binds to the protein. When ANS binds in the hydrophobic HSA binding sites [36,38], the ANS absorption spectrum (Fig. S1C, SI) becomes red-shifted by ~5 nm. The interaction between HSA and ANS was modelled using MCR-ALS of the absorption spectra to extract the concentration and pure spectral profiles of the individual species. Three species were extracted corresponding to: free ANS, free HSA, and a mixture of HSA-ANS complexes (Fig. S2, SI). The MCR model showed the decrease (from 1.50×10^{-4} M to 8.54×10^{-5} M at ~[HSA]/[ANS] = 10) in free HSA contribution and increase in free ANS contribution (~0 M up to ~[HSA]/[ANS] = 2 (all bound to HSA) increases to 7.4×10^{-5} M at [HSA]/[ANS] = 10) as ANS was added. The third extracted component corresponded to a combination of the different HSA-ANS complexes formed. A Job's plot [59,60], also known as method of continuous variation, is a common method used to determine binding stoichiometry and here, gives a 1:2 stoichiometry indicating at least two complexes are present (Table S1 & Fig. S3, SI).

$$J(\lambda) = \int_0^{\infty} F_D(\lambda)\varepsilon_A(\lambda)\lambda^4 d\lambda \tag{3}$$

where ε_A = extinction coefficient spectrum of the acceptor ($M^{-1}\ cm^{-1}$), λ = wavelength (nm) and F_D = donor emission spectrum normalized to an area of 1.

$$R_0 = 0.211 \times \left[\frac{\kappa^2 . \phi_D . J(\lambda)}{\eta^4}\right]^{1/6} \tag{4}$$

where, with R_0 in Å, κ^2 = orientation factor between the donor and acceptor, η = refractive index, ϕ_D = quantum yield of the donor in absence of the acceptor and J = overlap integral.

Comparison of band shapes showed a clear difference between parallel and perpendicular polarized excitation profiles of the directly excited, bound ANS (Fig. 3, peak c). The shoulder at ~350 nm in the excitation spectrum was stronger in the t-EEM$_\perp$ spectra and may be due to a larger contribution from ANS bound in secondary binding sites of HSA. This blue shift could indicate that these sites, which yield a more heterogeneous population of ANS fluorophores, may be more hydrophobic in nature [37].

3.2. Aniso-t-EEM maps and anisotropy analysis

As FRET causes emission depolarization [6,61,62], the *aniso*-t-EEM maps (bottom row, Fig. 2) can provide a clearer visualisation of FRET processes than the EEM spectra. Here, the *aniso*-t-EEMs clearly show ANS emission depolarisation ($\lambda_{ex}/\lambda_{em}$ = 250–310/420–550 nm), caused by hetero-FRET from the HSA donor (mostly Trp) to ANS. There is also depolarization of intrinsic HSA emission ($\lambda_{ex}/\lambda_{em}$ = 250–300/290–390 nm) as consequence of both intrinsic homotransfer-FRET (homo-FRET), Tyr-Tyr, and hetero-FRET (Tyr-Trp) [63,64]. The *aniso*-t-EEMs also provides information about ANS binding from the variation observed in the directly excited ANS emission region ($\lambda_{ex}/\lambda_{em}$ = 320–420/420–550 nm). When ANS first binds, at low molar ratios, to HSA, the emission anisotropy is more homogenous, whereas at higher ANS molar ratios ([ANS]/[HSA] > 1), more variation is observed in the anisotropy maps. ANS binds to HSA with two different binding modes [37]: first occupying the Sudlow II site (Fig. 1A) (r = 4.85 nm) with high affinity, leading to a more homogenous anisotropy observed across the emission space and second, as more ANS is added, secondary binding sites are occupied in a more non-specific character, generating anisotropy variation across the emission [36,38]. As the secondary HSA binding sites are occupied, emission becomes more depolarised due to ANS homo-FRET [65,66]. Furthermore, in these lower affinity sites, ANS is less strongly bound, than in the Sudlow II site, thus facilitating rotational depolarization [67].

3.3. HSA-ANS interaction modelling

Conventional spectroscopic analysis allows investigation of the HSA-ANS interaction via: *(i)* the decrease of overall HSA donor fluorescence due to quenching via FRET, *(ii)* the increase in ANS acceptor fluorescence due to both hydrophobic binding and FRET from HSA, *(iii)* the increase in the anisotropy of directly excited acceptor upon binding, *(iv)* the decrease in the anisotropy of the indirectly excited acceptor, and *(v)* the increase in donor anisotropy due to the shortening of the donor fluorescence lifetime. However, as the various fluorophore spectra all overlap, spectral unmixing methods are required in order to resolve the individual emission contributions. From a theoretical aspect, fluorescence emission from HSA-ANS complexes should have three main elements: component one, donor emission (HSA), component two, acceptor emission due to direct excitation (ANS), and component three, acceptor emission arising from indirect excitation (via FRET). The first two components are expected to have linearly independent loadings in all three modes, however component three was expected to comprise of donor excitation and acceptor emission. Here, a priori chemical knowledge was used to constrain the Tucker3 core array, extracting

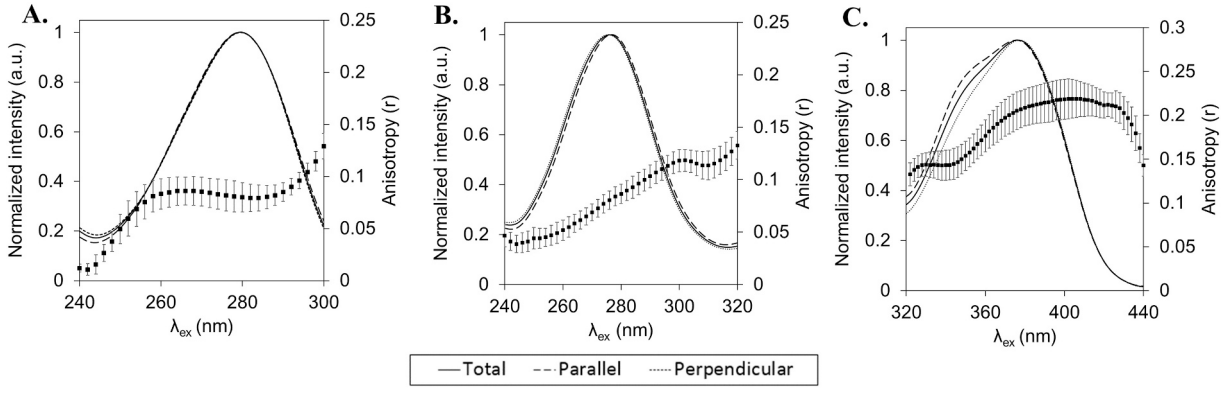

Fig. 3. Normalized excitation spectra for a representative [ANS]/[HSA] =1 sample of each of the different polarization measurements and corresponding emission anisotropy of: **(A)** peak a, λ_{em} = 350 nm, intrinsic HSA fluorescence; **(B)** peak b, λ_{em} = 470 nm, ANS bound to HSA fluorescence, direct & indirect emission; and, and **C)** peak c, λ_{em} = 470 nm, ANS fluorescence bound to HSA, direct emission only. The shoulder observed at ~350 nm in the excitation spectrum was stronger in the t-EEM$_\perp$ spectra.

fewer components in non-full rank modes (i.e. excitation and emission modes). A 3 × 2 × 2 core array, corresponding to concentration (1st), emission (2nd), and excitation (3rd) modes respectively, was selected. Singular value decomposition (SVD) of the unfolded three-way array in all three modes (**Fig. S4, SI**) showed between 2 and 4 components were present (or more correctly resolvable), but with a long tail. Photophysically we know that there are many more emitters (e.g. multiple Tyr residues), but the dataset (sample numbers, spectral resolution, and signal to noise) is not good enough for resolving the wider population of weak emitters.

A variety of different Tucker models were evaluated, constraining the core array which contains 12 possible interaction terms to just 3 or 4 (Fig. S5, SI). In model 1 the emission of indirectly excited ANS was set as the sole source of the third component (i.e. interaction term in excitation of donor and emission of acceptor). Models 2 and 3 allowed that in addition to indirectly excited ANS, the fluorescence of HSA or bound directly excited ANS were the sources of the third component. Finally, model 4 examined the possibility that there was no FRET derived emission and that the third component was composed of a mixture of directly excited emission from HSA and ANS. The most stable solution was achieved using model 1, and TuckCorCon [68], used to validate the obtained solution gave values of >99% in each mode, indicated a good model fit. Using a 3 × 2 × 2 Tucker3 model we extracted three species (Table 1) corresponding to: HSA emission comprised of unresolved Tyr and Trp emission, directly excited ANS emission, and ANS emission arising from indirect excitation via FRET (Fig. 4A-C, respectively).

Comparison (Fig. 5A-C) of the obtained scores and anisotropy values showed that the t-EEM$_T$ model was not as good at recovering the third component as the perpendicularly polarized emission data, and the perpendicular polarized data based models produced a more acceptable result. Significant differences were observed in components 2 and 3 between the t-EEM$_\perp$ and t-EEM$_\parallel$ data (Table 1), with more directly excited ANS observed in the parallel polarization (Fig. 5E) and more indirectly excited ANS observed in the perpendicular polarization (Fig. 5F). This suggests that perpendicular polarization measurements were more sensitive to the indirectly excited acceptor emission presumably because of the FRET orientation factor and the hindered nature of the fluorophores involved [62,63]. Validating this will require investigation of more controlled, rigid sample systems which is outside the scope of this current study. However, this chemometric separation of indirect and direction acceptor emission is of significance in understanding the complex non-linear emission and variation in anisotropy of interacting multi-fluorophore mixtures.

The recovered anisotropy values (Fig. 5A-C) provide another insight into the interaction process and a novel way of assessing the Tucker3 solutions. HSA anisotropy increased slightly at higher ANS concentrations (ANS/HSA > 2) as the emission becomes quenched consistent with FRET donor behaviour [6,7]. The bound ANS emission from direct excitation had a higher anisotropy (r ~ 0.2) at low molar ratios of ANS (ANS/HSA < 2), which then decreased to r ~ 0.18, possibly as a consequence of homo-FRET/ exciplex formation at higher ANS concentrations [65,69–72]. ANS emission anisotropy arising from indirect excitation via FRET was negative [7,73,74] presumably due to a combination of hindered motion and the relative orientations of donor and acceptor dipoles. However, the anisotropy values recovered for component 3 (indirectly excited ANS) are not reliable, as this component was poorly resolved in the parallel polarization dataset. Higher resolution datasets for chemometric analysis requires both lower noise spectra (i.e. averaged spectra from multiple repeat measurements) and higher sample numbers. This is not feasible with the current scanning-based systems and full pTSFS or pEEM spectral measurements because of the time required.

Table 1
Comparison of band maxima for the extracted components, component scores, and model fit parameters obtained from the 3 × 2 × 2 restricted Tucker3 models of the HSA-ANS system.

Polarization setting	t-EEM$_\parallel$	t-EEM$_\perp$	t-EEM$_T$
TuC1 (*HSA*): $\lambda_{ex}/\lambda_{em}$ (nm)	280/342	280/342	280/344
TuC1: Fit model (%)	4.4	4.6	9.7
TuC2 (*ANS*): $\lambda_{ex}/\lambda_{em}$ (nm)	274/474	274/474	274/474
TuC2: Fit model (%)	94.7	81.9	87.1
TuC3 (ANS via *FRET*): $\lambda_{ex}/\lambda_{em}$ (nm)	280/474	280/474	280/474
TuC3: Fit model (%)	0.9	13.5	3.2
Variance explained (%)	99.70	99.70	99.86
TuckCorCon (%)	99.96	99.96	100.00

Unlike the restricted Tucker3 model, PARAFAC could not deal with this very non-trilinear FRET based system as shown by model quality parameters and the recovered components (**Table S2, SI**). PARAFAC could not resolve the indirectly and directly excited ANS emission, however, the significant difference in the recovered components for each polarization measurement supported the restricted Tucker3 results. In the PARAFAC solution the core consistency (a test used to assess the validity of PARAFAC models) had a low value for the t-EEM$_\parallel$ based model but a negative value for the t-EEM$_\perp$ model. This suggests, a larger deviation from trilinear behaviour for the t-EEM$_\perp$ data which we suggest is caused by the greater fraction of indirectly excited ANS emission being measured in the perpendicular polarization.

3.4. Donor emission modelling

Intrinsic HSA fluorescence emission arises from several fluorescent contributions: *(i)* directly excited Tyr, *(ii)* directly excited Trp, *(iii)* indirectly excited Trp, from Tyr-Trp hetero-FRET, and *(iv)* indirectly excited Tyr (homo-FRET) [2,7]. However, it is unreasonable to expect that chemometric modelling could resolve all these components with this dataset. Here, we aim to resolve the HSA emission into two components: Tyr which is mostly non-interacting in FRET with ANS, and Trp, which has a strong FRET interaction with ANS. Changes in the intrinsic HSA emission ($\lambda_{ex}/\lambda_{em}$ = 250–310/290–390 nm, peak A, Fig. 2) were evaluated in each polarization mode using PARAFAC models at varying [ANS]/[HSA] molar ratios. These models show the quenching and emission spectral blue shifts of the intrinsic Tyr and Trp fluorophores (Fig. S6 & Table S3, SI) during ANS binding. In all cases, PARAFAC analysis of intrinsic HSA fluorescence recovered two components (explaining >99% of the total variance) for each polarization mode (Table 2) and the quality parameters indicated that these components behaved in a trilinear fashion. PARAFAC Component 1 (PaC1, 83–86% explained variance) is mostly Trp-214 emission, which is linked to ANS by FRET. PARAFAC Component 2 (PaC2, 14–17% explained variance) was related to Tyr emission. The non-linear correlation (Fig. S7, SI) between the shift in the HSA emission maximum with the changing ratio of the resolved PARAFAC components (PaC1/PaC2), may be due to different quenching mechanisms operating for the Tyr and Trp fluorophores.

The anisotropy values calculated (Fig. 6) for the recovered components can be used to confirm the accuracy of the resolved components for the small molecule case [76]. Here, with FRET effects, this is less certain but the values, $r = 0.09 \pm 0.01$ for Trp and $r = 0.14 \pm 0.01$ for Tyr (at [ANS]/[HSA] = 1) are consistent with values cited in the literature [76,77]. The slight increase in anisotropy, observed for both Trp (PaC1) and Tyr (PaC2), at higher ANS molar ratios of (>2) was ascribed to reductions in lifetime because of quenching and FRET processes [7].

3.5. Stern-Volmer analysis

Stern-Volmer and modified Stern-Volmer (SI) were used to quickly assess sample suitability for accurate FRET over the full sample set range. Specifically, one needs to identify the onset of interfering

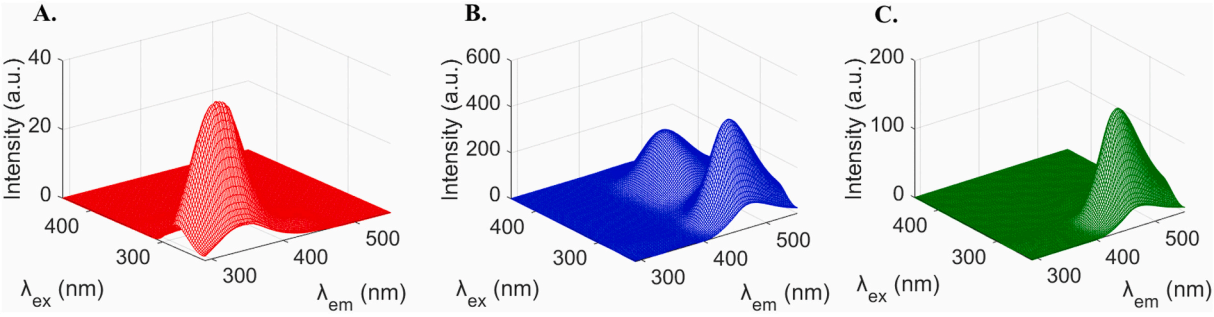

Fig. 4. Components recovered from restricted Tucker3 modelling of full HSA-ANS emission, a representative example shown for [ANS]/[HSA] = 1 for the most stable t-EEM$_\perp$ model. The components recovered correspond to: **(A)** Intrinsic HSA emission (composed of Tyr & Trp); **(B)** ANS emission arising from direct excitation; and **(C)** ANS emission arising from indirect excitation (via FRET).

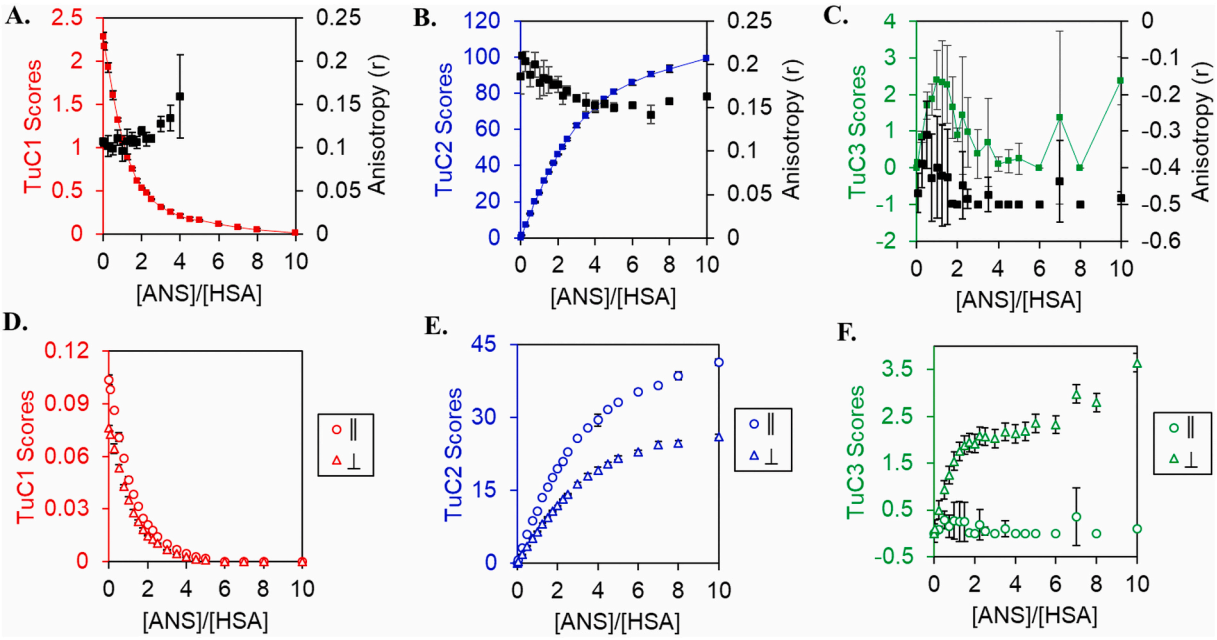

Fig. 5. Plots of Scores (relative concentrations) and anisotropy values against [ANS]/[HAS] ratios recovered using 3 × 2 × 2 restricted Tucker3 models. **(First row)** t-EEM$_T$ model: **(A)** Component 1, HSA intrinsic emission quenched by addition of ANS; **(B)** Component 2, ANS emission from direct excitation; **(C)** Component 3, ANS emission arising via indirect excitation by FRET (this is an unstable component). **(Second row)***t*-EEM$_\perp$ and *t*-EEM$_\parallel$ models for: **(D)** Component 1; **(E)** Component 2; and **(F)** Component 3 (stable component in *t*-EEM$_\perp$).

Table 2
Comparison of model parameters and components obtained for PARAFAC modelling of intrinsic HSA donor emission from the different polarization measurements.

Polarization setting	t-EEM$_\parallel$	t-EEM$_\perp$	t-EEM$_T$
PaC1 $\lambda_{ex}/\lambda_{em}$ (nm)	280/354	280/356	280/354
PaC1 Fit model (%)	82.9	85.8	85.3
PaC2 $\lambda_{ex}/\lambda_{em}$ (nm)	278/308	276/310	278/308
PaC2 Fit model (%)	17.1	14.2	14.7
Variance explained (%)	99.94	99.95	99.94
CONCORDIA (%)	99.47	99.30	99.55
Split-half analysis (%)	99.74	99.22	99.45

quenching effects due to the presence of increasing amounts of unbound ANS. Stern-Volmer plots (Fig. S8A, SI) produced using the PARAFAC resolved Tyr and Trp components were significantly different than those generated using conventional spectra. The Stern-Volmer quenching constants (K_{SV}) were significantly higher (~16%) when calculated using PARAFAC scores (Table 3) for Trp compared to using normal unresolved emission data. The large differences between the Trp and Tyr K_{SV} values reflects the different quenching mechanisms at play [7,78–80].

Over the wider ANS concentration range, PaC1 scores showed that Trp-214 underwent three phases of quenching (Fig. S8 A-D, SI). Firstly, a linear relationship was observed up to a 1:1 ANS/HSA ratio indicative of a single fully collisional quenching process [6,7]. This can be attributed to ANS induced quenching [36,38]. As more ANS was added ([ANS]/[HSA] > 1) the Stern-Volmer plot first curves upward which is symptomatic of a more complex quenching process due to the presence of increasing amounts of static quenching or a second dynamic quenching process. These changes in fluorescence emission were further examined using a modified Stern-Volmer analysis [7,81–84] over the full sample range (Fig. S9, SI). This shows much more complex behaviour for [ANS] > 2.0×10^{-5} M was due to increasing ANS occupancy of the secondary

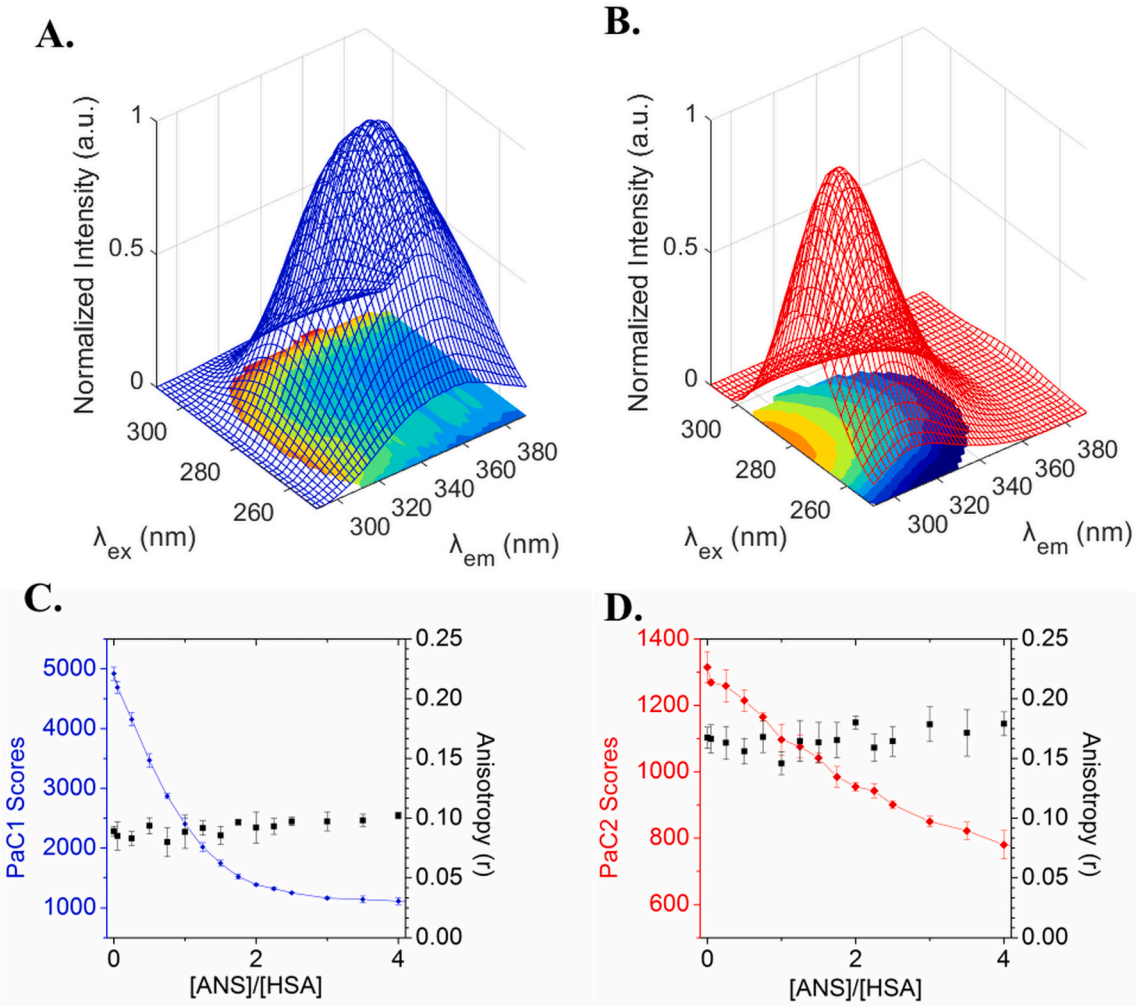

Fig. 6. Normalized PARAFAC components of: (A) Trp (PaC1); and (B) Tyr (PaC2), obtained from decomposition of intrinsic HSA fluorescence (representative example shown for [ANS]/[HSA] = 1) with the anisotropy maps shown under the signal (colour bar indicates corresponding anisotropy values of map). (C-D) PARAFAC scores (relative concentrations for *t*-EEM$_T$) and anisotropy values (with standard deviation of triplicate samples) of a single point at emission maximum of: (C) PaC1, $\lambda_{ex}/\lambda_{em}$ = 280/354 nm; and (D) PaC2, $\lambda_{ex}/\lambda_{em}$ = 278/308 nm, for all samples (n = 63).

Table 3
Stern-Volmer quenching constants calculated using the unresolved fluorescence emission (classical) and resolved Trp (PaC1) and Tyr (PaC2) emission, for the appropriate linear region (up to [ANS]/[HSA] = 1).

Polarization	t-EEM$_{\parallel}$	t-EEM$_{\perp}$	t-EEM$_T$
Classical Stern-Volmer	F_0/F at $\lambda_{ex}/\lambda_{em}$ 280/350 nm		
K_{SV} ($\times 10^4$ M^{-1})	6.0 ± 0.4	6.1 ± 0.5	6.0 ± 0.4
r^2	0.98 ± 0.01	0.99 ± 0.01	0.99 ± 0.01
Trp (PaC1)	PaC1$_0$/PaC1		
K_{SV} ($\times 10^4$ M^{-1})	7.2 ± 0.5	7.1 ± 0.4	7.1 ± 0.5
r^2	0.98 ± 0.00	0.98 ± 0.01	0.98 ± 0.01
Tyr (PaC2)	PaC2$_0$/PaC2		
K_{SV} ($\times 10^4$ M^{-1})	1.5 ± 0.1	1.1 ± 0.2	1.2 ± 0.2
r^2	0.89 ± 0.09	0.87 ± 0.15	0.88 ± 0.07

binding sites, inner filter effects, and other interactions. Resolving these effects and their relative contributions would necessitate collecting data at different temperatures which is outside the scope of this work. From [ANS]/[HSA] = 2 to [ANS]/[HSA] = 4, static quenching of Trp-214 emission was observed which was consistent with fluorescence lifetime measurements (Fig. S10 & Table S5, SI), where the τ/τ_0 value was nearly constant for [ANS]/[HSA] >2. For [ANS]/[HSA] > 4, Trp emission was relatively constant indicating that quenching was maximised, and no further changes can be discriminated. For the Stern-Volmer plot using PaC2 scores (Tyr emission), we saw an almost linear decrease caused by quenching up to [ANS]/[HSA] = 4 ($r^2 > 0.99$) indicating a single type of static quenching, because the lifetime was essentially constant for [ANS]/[HSA] >2 [6,7]. The most important outcome of the Stern-Volmer analysis is that the sample range for FRET calculations has to be restricted to those samples with [ANS]/[HSA] ratios of <1, to avoid bias due to these other processes.

3.6. Multivariate calculation of FRET efficiency

Finally, using the PARAFAC solution obtained, a new method was proposed to calculate FRET efficiency in a multi-dimensional manner. Commonly FRET efficiency is calculated using a single point of the unresolved donor emission (here, intrinsic HSA fluorescence) from 2-D spectra [6–8]. Thus, the maximum emission of the FRET donor in the presence of the acceptor (F_{DA}) and in the absence of the acceptor (F_D) are used to calculate FRET efficiency using Eq. (5).

$$E = 1 - \frac{F_{DA}}{F_D} \tag{5}$$

The conventional method, however, does not account for the presence of emission from non-interacting fluorophores (PaC2). PARAFAC decomposition of the donor quenching process enables calculation of FRET efficiency using the interacting species only (PaC1). Our new

proposed method replaces the intensity measurements with the recovered components $PaC1_{DA}$ and $PaC1_{D}$ (Eq. (6)).

$$E = 1 - \frac{PaC1_{DA}}{PaC1_{D}} \quad (6)$$

PARAFAC resolution of intrinsic HSA (donor) fluorescence, enabled FRET efficiency calculations using the multi-dimensional emission of the interacting component only. FRET efficiency values calculated using the new proposed PARAFAC method consistently show higher (of up to ~2–3%), but statistically significant absolute values (p-value <0.05) for the [ANS]/[HSA] 1.0 > 0.25 samples) than those calculated conventionally using the single point calculations from the unresolved raw t-EEM (Table 4). The underestimation of the Trp-ANS FRET efficiency using conventional 2D spectra is due to the quenching of the non-interacting Tyr residues whose emission overlaps that of the FRET interacting species. Although the difference observed in this example are small, larger differences would be observed in cases where non-interacting fluorophores had higher quantum yields. The FRET efficiencies recovered from the Tucker3 modelling which follow the same trends are included for comparison, although, these cannot be relied upon as the Tucker 3 model was not ideal. The Tucker3 derived values were also significantly higher than the conventional values, and slightly higher than the PARAFAC derived values. This may be due to the fact that the Tucker component used for calculation comprises both Trp and Tyr emission whereas the PARAFC component represents only the Trp emission. In addition, the contribution of the HSA donor emission is very small relative to the overall emission, so this model was less likely to accurately assess donor emission as it becomes quenched. At higher ratios of [ANS]/[HSA] >2.5, where HSA is more quenched, very little signal is resolved leading to unreasonably high values of FRET efficiencies, the values at lower concentrations of ANS are in better agreement with PARAFAC results.

4. Conclusions

The feasibility of using ARMES [17,18] to study FRET has been demonstrated and the chemometric resolution of the fluorescence emission into its constituent components facilitated a more accurate analysis of molecular interactions and photophysical processes. Restricted Tucker3 modelling of the t-EEM spectra from this HSA-ANS system was able to effectively deal with the non-linearity in the acceptor spectral region [25,26]. This enabled the resolution of the fluorescence emission into three emission components [9,10,25]: intrinsic HSA (Tyr + Trp), directly excited ANS, and ANS indirectly excited via FRET. A large difference between the polarization measurements was observed in the amount of emission attributed to indirect ANS excitation, with the perpendicular polarization showing a higher intensity. Furthermore, the extracted component anisotropy information along with the *aniso*-EEM plots provide additional information for assessing the quality of the multivariate resolution and for investigating the FRET processes [62,66] occurring in the HSA-ANS model system. Under these experimental conditions however we were not able (or expect) to be able to clearly resolve all the different emitting components and enable the analysis of the more subtle, yet important, Tyr homotransfer, HSA-ANS at binding site 1; HSA-ANS to binding site 2, and ANS-ANS homotransfer effects. To do so would require a different experimental system where the excess unbound ANS was removed, the data acquired with much better signal to noise, and a higher number of samples in the dataset to enable more effective chemometric modelling. The ability to resolve the indirectly excited ANS emission from directly excited ANS, is potentially significant for studying the non-linear fluorescence behaviour of other spectrally overlapped multi-fluorophore protein systems.

Furthermore, PARAFAC [19] modelling of the intrinsic HSA (donor) fluorescence allowed discrimination of FRET interacting (Trp-214) and non-interacting (Tyr) fluorophores. The resolution of the different fluorophore emissions enabled the more accurate calculation of Stern-Volmer quenching constants and FRET efficiencies using these relatively simple multi-dimensional emission measurements. The Stern-Volmer quenching constants calculated using the resolved Tyr and Trp emission showed larger differences (~16–21%) compared to conventional spectral based measurements [6–8]. Stern-Volmer analyses were also used to identify the range of appropriate samples (i.e. [ANS]/[HSA] ratios of <1) which were free from interfering quenching processes and thus could be used for accurate FRET calculations. FRET efficiency values for the appropriate samples calculated using the FRET interacting, Trp, component gave significantly higher absolute values (~2–3%) than the conventional analysis based on the use of simple 2D spectra which tend to underestimate FRET efficiencies because of the emission overlap between interacting and non-interacting fluorophores. This translates into a 6–7% relative increase which is potentially important for quantitative analyses. For the higher [ANS]/[HSA] ratios >1, the influence of other quenching processes in this sample system with excess free ANS in solution make E_T value calculations unreliable, even though component resolution is still feasible using PARAFAC and Tucker 3.

This multivariate analysis of the HSA-ANS model system shows the potential for ARMES to be used to study FRET in more complex multi-fluorophore proteins and macromolecular systems. We are continuing to refine the methodology because component resolution, and thus the accuracy of calculated parameters such as quenching constants is closely

Table 4
FRET efficiency values (mean and standard deviation (in brackets)) calculated for each polarization measurement using the conventional, PARAFAC, and Tucker3 methods. Conventional calculations were made using at $\lambda_{ex}/\lambda_{em}$ = 280/350 nm (from t-EEM spectra). Values for [ANS]/[HSA] ratios of >1 are unreliable due to the increasing influence of other quenching processes as identified by Stern-Volmer analysis.

	Conventional $\left(E = 1 - \frac{F_{DA}}{F_{D}}\right)$			PARAFAC $\left(E = 1 - \frac{PaC1_{DA}}{PaC1_{D}}\right)$			Tucker 3			*t*-test values (conv./PARAFAC)		
ANS/HSA	$EEM_{\parallel}$	$EEM_{\perp}$	EEM_{T}	$EEM_{\parallel}$	$EEM_{\perp}$	EEM_{T}	$EEM_{\parallel}$	$EEM_{\perp}$	EEM_{T}	$EEM_{\parallel}$	$EEM_{\perp}$	EEM_{T}
0.05	0.050 (0.01)	0.045 (0.02)	0.047 (0.02)	0.051 (0.02)	0.045 (0.02)	0.047 (0.02)	0.052 (0.01)	0.047 (0.02)	0.048 (0.02)	0.747	0.929	0.888
0.25	0.16 (0.01)	0.14 (0.03)	0.15 (0.02)	0.16 (0.01)	0.15 (0.03)	0.16 (0.02)	0.17 (0.01)	0.16 (0.04)	0.16 (0.02)	0.0094	0.284	0.007
0.5	0.29 (0.03)	0.27 (0.02)	0.28 (0.02)	0.31 (0.02)	0.29 (0.02)	0.30 (0.02)	0.32 (0.02)	0.30 (0.02)	0.30 (0.02)	0.011	0.041	0.002
1	0.50 (0.02)	0.48 (0.03)	0.49 (0.02)	0.52 (0.02)	0.51 (0.02)	0.51 (0.02)	0.55 (0.02)	0.54 (0.02)	0.52 (0.02)	0.004	0.040	0.001
2.5	*0.72 (0.00)*	*0.72 (0.00)*	*0.72 (0.00)*	*0.75 (0.00)*	*0.75 (0.00)*	*0.75 (0.00)*	*0.86 (0.00)*	*0.86 (0.00)*	*0.82 (0.00)*	0.001	0.003	0.001
5	*0.75 (0.00)*	*0.75 (0.01)*	*0.75 (0.01)*	*0.76 (0.00)*	*0.77 (0.01)*	*0.77 (0.01)*	*0.98 (0.00)*	*0.99 (0.00)*	*0.93 (0.01)*	0.001	0.001	0.004
10	*0.71 (0.01)*	*0.73 (0.01)*	*0.72 (0.01)*	*0.73 (0.01)*	*0.75 (0.01)*	*0.75 (0.01)*	*1.00 (0.00)*	*1.00 (0.00)*	*0.99 (0.01)*	0.0010	0.0020	0.0038

Note: paired t-test conducted at 95% confidence interval for FRET efficiency calculations based on conventional and proposed PARAFAC approach for each polarization measurement.

linked to sample number and signal-to-noise ratio. This becomes more critical when the number of protein fluorophores involved increases as we have shown for IgG [14]. However, for protein-ligand interactions where there are relatively low numbers of fluorophores involved in the FRET system, ARMES offers an alternative, relatively inexpensive methodology for quantifying FRET effects. Finally, this multi-dimensional measurement and analysis approach can be further extended to make use of the scattered light component of pEEM measurements to simultaneously provide information about protein size changes caused by oligomerisation or aggregation [15,16,85].

Credit author statement

Fiona Gordon: designed and performed the experiments, analysed the data, and wrote the original draft. Saioa Elcoroaristizabal: analysed the data and edited the manuscript. **Alan Ryder:** conceptualization, supervision, **funding acquisition, reviewed** and edited the manuscript.

Declaration of Competing Interest

The authors declare no conflicts of interest.

Acknowledgements

This publication has emanated from research supported in part by a research grant from Science Foundation Ireland and is co-funded under the European Regional Development Fund under Grant number (14/IA/2282, *Advanced Analytics for Biological Therapeutic Manufacture*, to AGR). We also thank Agilent Technologies (Mulgrave Victoria, Australia) for the loan of a fluorescence spectrometer.

Appendix A. Supplementary data

Supplementary data to this article can be found online at https://doi.org/10.1016/j.bbagen.2020.129770.

References

[1] Förster, Zwischenmolekulare energiewanderung und fluoreszenz, Ann. Phys. 437 (1948) 55–75.
[2] A.B.T. Ghisaidoobe, S.J. Chung, Intrinsic tryptophan fluorescence in the detection and analysis of proteins: a focus on forster resonance energy transfer techniques, Int. J. Mol. Sci. 15 (2014) 22518–22538.
[3] M.C. Murphy, I. Rasnik, W. Cheng, T.M. Lohman, T.J. Ha, Probing single-stranded DNA conformational flexibility using fluorescence spectroscopy, Biophys. J. 86 (2004) 2530–2537.
[4] L. Yuan, W.Y. Lin, K.B. Zheng, S.S. Zhu, FRET-based small-molecule fluorescent probes: rational design and bioimaging applications, Acc. Chem. Res. 46 (2013) 1462–1473.
[5] L. Stryer, Fluorescence energy transfer as a spectroscopic ruler, Annu. Rev. Biochem. 47 (1978) 819–846.
[6] B. Valeur, Molecular Fluorescence: Principles and Applications, 2nd edition, John Wiley & Sons, 2002.
[7] J.R. Lakowicz, Principles of Fluorescence Spectroscopy, 3rd ed., Springer, New York, 2006.
[8] T.W.J. Gadella, FRET and FLIM techniques, Elsevier Science, 2011.
[9] A.D. Hoppe, B.L. Scott, T.P. Welliver, S.W. Straight, J.A. Swanson, N-way FRET microscopy of multiple protein-protein interactions in live cells, PLoS One 8 (2013).
[10] S. Mustafa, J. Hannagan, P. Rigby, K. Pfleger, B. Corry, Quantitative forster resonance energy transfer efficiency measurements using simultaneous spectral unmixing of excitation and emission spectra, J. Biomed. Opt. 18 (2013), 026024–026021 - 026024-026014.
[11] G.W. Gordon, G. Berry, X.H. Liang, B. Levine, B. Herman, Quantitative fluorescence resonance energy transfer measurements using fluorescence microscopy, Biophys. J. 74 (1998) 2702–2713.
[12] I.M. Warner, G.D. Christian, E.R. Davidson, J.B. Callis, Analysis of multicomponent fluorescence data, Anal. Chem. 49 (1977) 564–573.
[13] D. Patra, A.K. Mishra, Recent developments in multi-component synchronous fluorescence scan analysis, TrAC Trends Anal. Chem. 21 (2002) 787–798.
[14] M. Steiner-Browne, S. Elcoroaristizabal, A.G. Ryder, Using polarized total synchronous fluorescence spectroscopy (pTSFS) with PARAFAC analysis for characterizing intrinsic protein emission, Chemom. Intell. Lab. Syst. 194 (2019), 103871.
[15] A.L. de Faria e Silva, S. Elcoroaristizabal, A.G. Ryder, Multi-attribute quality screening of immunoglobulin G using polarized excitation emission matrix spectroscopy, Anal. Chim. Acta 1101 (2020) 99–110.
[16] A.L. de Faria e Silva, S. Elcoroaristizabal, A.G. Ryder, Characterization of lysozyme PEGylation products using polarized excitation-emission matrix spectroscopy, Biotechnol. Bioeng. 117 (2020) 2969–2984.
[17] R.C. Groza, B.Y. Li, A.G. Ryder, Anisotropy resolved multidimensional emission spectroscopy (ARMES): a new tool for protein analysis, Anal. Chim. Acta 886 (2015) 133–142.
[18] Y. Casamayou-Boucau, A.G. Ryder, Extended wavelength anisotropy resolved multidimensional emission spectroscopy (ARMES) measurements: better filters, validation standards, and Rayleigh scatter removal methods, Methods Appl. Fluoresc. 5 (2017), 037001.
[19] R. Bro, PARAFAC. Tutorial and applications, Chemom. Intell. Lab. Syst. 38 (1997) 149–171.
[20] C.A. Stedmon, S. Markager, R. Bro, Tracing dissolved organic matter in aquatic environments using a new approach to fluorescence spectroscopy, Mar. Chem. 82 (2003) 239–254.
[21] H. Chen, J.E. Kenny, Application of PARAFAC to a two-component system exhibiting fluorescence resonance energy transfer: from theoretical prediction to experimental validation, Analyst 137 (2012) 153–162.
[22] L.R. Tucker, Some mathematical notes on three-mode factor analysis, Psychometrika (1966) 279–311.
[23] P.M. Kroonenberg, J.M.F. ten Berge, The equivalence of Tucker3 and Parafac models with two components, Chemom. Intell. Lab. Syst. 106 (2011) 21–26.
[24] Y. Akhlaghi, M. Kompany-Zareh, S. Ebrahimi, Model-based approaches to investigate the interactions between unmodified gold nanoparticles and DNA strands, Sens. Actuator B-Chem. 221 (2015) 45–54.
[25] Y. Akhlaghi, M. Kompany-Zareh, M.R. Hormozi-Nezhad, Multiway investigation of interaction between fluorescence labeled DNA strands and unmodified gold nanoparticles, Anal. Chem. 84 (2012) 6603–6610.
[26] M. Kompany-Zareh, S. Gholami, Soft and hard multiway FRET-based investigation of interaction between drug and QD labeled DNA, Chemom. Intell. Lab. Syst. 139 (2014) 33–41.
[27] C.M. Yengo, C.L. Berger, Fluorescence anisotropy and resonance energy transfer: powerful tools for measuring real time protein dynamics in a physiological environment, Curr. Opin. Pharmacol. 10 (2010) 731–737.
[28] A.L. Mattheyses, A.D. Hoppe, D. Axelrod, Polarized fluorescence resonance energy transfer microscopy, Biophys. J. 87 (2004) 2787–2797.
[29] D.M. Togashi, A.G. Ryder, A fluorescence analysis of ANS bound to bovine serum albumin: binding properties revisited by using energy transfer, J. Fluoresc. 18 (2008) 519–526.
[30] D.M. Togashi, A.G. Ryder, D. O'Shaughnessy, Monitoring local unfolding of bovine serum albumin during denaturation using steady-state and time-resolved fluorescence spectroscopy, J. Fluoresc. 20 (2010) 441–452.
[31] M.L. Ferrer, R. Duchowicz, B. Carrasco, J.G. de la Torre, A.U. Acuna, The conformation of serum albumin in solution: a combined phosphorescence depolarization-hydrodynamic modeling study, Biophys. J. 80 (2001) 2422–2430.
[32] T. Peters, Serum albumin, Adv. Protein Chem. 37 (1985) 161–245.
[33] O.K. Gasymov, B.J. Glasgow, ANS fluorescence: potential to augment the identification of the external binding sites of proteins, Bba-Proteins Proteom. 1774 (2007) 403–411.
[34] R. Joshi, M. Jadhao, H. Kumar, S.K. Ghosh, Is the Sudlow site I of human serum albumin more generous to adopt prospective anti-cancer bioorganic compound than that of bovine: a combined spectroscopic and docking simulation approach, Bioorg. Chem. 75 (2017) 332–346.
[35] H. Kumar, V. Devaraji, R. Joshi, S. Wankar, S.K. Ghosh, A chalcone-based potential therapeutic small molecule that binds to subdomain IIA in HSA precisely controls the rotamerization of Trp-214, ACS Omega 3 (2018) 10114–10128.
[36] G. Sudlow, D.J. Birkett, D.N. Wade, The characterization of two specific drug binding sites on human serum albumin, Mol. Pharmacol. 11 (1975) 824–832.
[37] I.M. Kuznetsova, A.I. Sulatskaya, O.I. Povarova, K.K. Turoverov, Reevaluation of ANS binding to human and bovine serum albumins: key role of equilibrium microdialysis in ligand - receptor binding characterization, PLoS One 7 (2012) 9.
[38] L.A. Bagatolli, S.C. Kivatinitz, F. Aguilar, M.A. Soto, P. Sotomayor, G.D. Fidelio, Two distinguishable fluorescent modes of 1-anilino-8-naphthalenesulfonate bound to human albumin, J. Fluoresc. 6 (1996) 33–40.
[39] E.M. Kosower, D. Huppert, Excited state Electron and proton transfers, Annu. Rev. Phys. Chem. 37 (1986) 127–156.
[40] E.M. Kosower, Intramolecular donor-acceptor systems. 9. Photophysics of (phenylamino)naphthalenesulfonates: a paradigm for excited-state intramolecular charge transfer, Acc. Chem. Res. 15 (1982) 259–266.
[41] G. Weber, D.J.R. Laurence, Fluorescent indicators of adsorption in aqueous solution and on the solid phase, Biochem. J. 56 (1954) R31.
[42] A. Sulkowska, Interaction of drugs with bovine and human serum albumin, J. Mol. Struct. 614 (2002) 227–232.
[43] S.H.D. Lacerda, J.J. Park, C. Meuse, D. Pristinski, M.L. Becker, A. Karim, J. F. Douglas, Interaction of gold nanoparticles with common human blood proteins, ACS Nano 4 (2010) 365–379.
[44] M. Steiner-Browne, S. Elcoroaristizabal, Y. Casamayou-Boucau, A.G. Ryder, Investigating native state fluorescence emission of immunoglobulin G using polarized excitation emission matrix (pEEM) spectroscopy and PARAFAC, Chemom. Intell. Lab. Syst. 185 (2019) 1–11.
[45] D.N. Kothawala, K.R. Murphy, C.A. Stedmon, G.A. Weyhenmeyer, L.J. Tranvik, Inner filter correction of dissolved organic matter fluorescence, Limnol. Oceanogr. Methods 11 (2013) 616–630.

[46] K. Kumar, A.K. Mishra, Parallel factor (PARAFAC) analysis on total synchronous fluorescence spectroscopy (TSFS) data sets in excitation-emission matrix fluorescence (EEMF) layout: certain practical aspects, Chemom. Intell. Lab. Syst. 147 (2015) 121–130.
[47] M. Bahram, R. Bro, C. Stedmon, A. Afkhami, Handling of Rayleigh and Raman scatter for PARAFAC modeling of fluorescence data using interpolation, J. Chemom. 20 (2006) 99–105.
[48] J. Jaumot, R. Gargallo, A. de Juan, R. Tauler, A graphical user-friendly interface for MCR-ALS: a new tool for multivariate curve resolution in MATLAB, Chemom. Intell. Lab. Syst. 76 (2005) 101–110.
[49] Z.J. Cheng, R. Liu, X.H. Jiang, Spectroscopic studies on the interaction between tetrandrine and two serum albumins by chemometrics methods, Spectrochim. Acta A 115 (2013) 92–105.
[50] T. Azzouz, R. Tauler, Application of multivariate curve resolution alternating least squares (MCR-ALS) to the quantitative analysis of pharmaceutical and agricultural samples, Talanta 74 (2008) 1201–1210.
[51] S. Elcoroaristizabal, A. de Juan, J.A. Garcia, N. Durana, L. Alonso, Comparison of second-order multivariate methods for screening and determination of PAHs by total fluorescence spectroscopy, Chemometr. Intell. Lab. 132 (2014) 63–74.
[52] F.L. Hitchcock, The expression of a tensor or a polyadic as a sum of products, J. Math. Phys. 6 (1927).
[53] C.J. Carroll, J. D, Analysis of individual differences in multidimensional scaling via an N-way generalization of an 'Eckart-Young' decomposition, Psychometrika 35 (1970) 283–319.
[54] R.A. Harshman, Foundations of the parafac procedure: model and conditions for an 'explanatory' multi-mode factor analysis. , UCLA work. Pap, Phon. (1970) 1–84.
[55] L. Lenhardt, R. Bro, I. Zekovic, T. Dramicanin, M.D. Dramicanin, Fluorescence spectroscopy coupled with PARAFAC and PLS DA for characterization and classification of honey, Food Chem. 175 (2015) 284–291.
[56] H. Abdollahi, R. Tauler, Uniqueness and rotation ambiguities in multivariate curve resolution methods, Chemom. Intell. Lab. Syst. 108 (2011) 100–111.
[57] A. de Juan, R. Tauler, Comparison of three-way resolution methods for non-trilinear chemical data sets, J. Chemom. 15 (2001) 749–772.
[58] H.A.L. Kiers, Hierarchical relations among 3-way methods, Psychometrika 56 (1991) 449–470.
[59] J.S. Renny, L.L. Tomasevich, E.H. Tallmadge, D.B. Collum, Method of continuous variations: applications of job plots to the study of molecular associations in organometallic chemistry, Angew. Chem. Int. Ed. Eng. 52 (2013) 11998–12013.
[60] P. Job, Formation and stability of inorganic complexes in solution, Ann. Chim. 10 (1928) 113–203.
[61] G. E, P. P, Einfluss der konzentration auf die polarisation der fluoreszenz von farbstofflosenungen, Physik 24 (1924) 24–36.
[62] D.M. Jameson, J.A. Ross, Fluorescence polarization/anisotropy in diagnostics and imaging, Chem. Rev. 110 (2010) 2685–2708.
[63] G. Weber, Polarizaion of the fluorescence of macromolecules 1. Theory and experimental method, Biochem. J. 51 (1952) 145–155.
[64] P.D.J. Moens, M.K. Helms, D.M. Jameson, Detection of tryptophan to tryptophan energy transfer in proteins, Protein J. 23 (2004) 79–83.
[65] G. Weber, E. Daniel, Cooperative effects in binding by bovine serum albumin 2. Binding of 1-anilino-8-naphthalene sulfonate. Polarization of ligand fluorescence and quenching of protein fluorescence, Biochemistry 5 (1966), 1900-&.
[66] Z. Zolmajd-Haghighi, Q.S. Hanley, When one plus one does not equal two: fluorescence anisotropy in aggregates and multiply labeled proteins, Biophys. J. 106 (2014) 1457–1466.
[67] U. Kragh-Hansen, V.T.G. Chuang, M. Otagiri, Practical aspects of the ligand-binding and enzymatic properties of human serum albumin, Biol. Pharm. Bull. 25 (2002) 695–704.
[68] M. Kompany-Zareh, Y. Akhlaghi, R. Bro, Tucker core consistency for validation of restricted Tucker3 models, Anal. Chim. Acta 723 (2012) 18–26.
[69] T. Sen, S. Mandal, S. Haldar, K. Chattopadhyay, A. Patra, Interaction of gold nanoparticle with human serum albumin (HSA) protein using surface energy transfer, J. Phys. Chem. C 115 (2011) 24037–24044.
[70] D. Fuentealba, H. Kato, M. Nishijima, G. Fukuhara, T. Mori, Y. Inoue, C. Bohne, Explaining the highly enantiomeric photocyclodimerization of 2-Anthracenecarboxylate bound to human serum albumin using time-resolved anisotropy studies, J. Am. Chem. Soc. 135 (2013) 203–209.
[71] S. Zorrilla, G. Rivas, A.U. Acuna, M.P. Lillo, Protein self-association in crowded protein solutions: a time-resolved fluorescence polarization study, Protein Sci. 13 (2004) 2960–2969.
[72] F.N. Castellano, J.D. Dattelbaum, J.R. Lakowicz, Long-lifetime Ru(II) complexes as labeling reagents for sulfhydryl groups, Anal. Biochem. 255 (1998) 165–170.
[73] P. Sarkar, S.V. Koushik, S.S. Vogel, I. Gryczynski, Z. Gryczynski, Photophysical properties of cerulean and venus fluorescent proteins, J. Biomed. Opt. 14 (2009) 034047.
[74] X. Shi, J. Basran, H.E. Seward, W. Childs, C.R. Bagshaw, S.G. Boxer, Anomalous negative fluorescence anisotropy in yellow fluorescent protein (YFP 10C): quantitative analysis of FRET in YFP dimers, Biochemistry 46 (2007) 14403–14417.
[75] Y. Casamayou-Boucau, A.G. Ryder, Accurate anisotropy recovery from fluorophore mixtures using multivariate curve resolution (MCR), Anal. Chim. Acta 1000 (2018) 132–143.
[76] S. Khrapunov, N. Pastor, M. Brenowitz, Solution structural studies of the saccharomyces cerevisiae TATA binding protein (TBP) †, Biochemistry 41 (2002) 9559–9571.
[77] I.M. Vlasova, V.V. Zhuravleva, A.M. Saletsky, Denaturation of bovine serum albumin initiated by sodium dodecyl sulfate as monitored via the intrinsic fluorescence of the protein, Russ. J. Phys. Chem. B 8 (2014) 385–390.
[78] M. Song, S. Liu, J. Yin, H. Wang, Interaction of human serum album and C_{60} aggregates in solution, Int. J. Mol. Sci. 12 (2011) 4964–4974.
[79] I. Cvijetić, D. Petrovic, T. Verbić, I. Juranic, B. Drakulic, Human serum albumin binding of 2-[(Carboxymethyl)sulfanyl]-4-oxo-4-(4-tert-butylphenyl)butanoic acid and its mono-me Ester, ADMET & DMPK 2 (2014) 126–142.
[80] A.A. Salem, M. Lotfy, A. Amin, M.A. Ghattas, Characterization of human serum albumin's interactions with safranal and crocin using multi-spectroscopic and molecular docking techniques, Biochem. Biophys. Rep. 20 (2019), 100670.
[81] S. Lehrer, Solute perturbation of protein fluorescence. Quenching of the tryptophyl fluorescence of model compounds and of lysozyme by iodide ion, Biochemistry 10 (1971) 3254–3263.
[82] Z.-J. Cheng, H.-M. Zhao, Q.-Y. Xu, R. Liu, Investigation of the interaction between indigotin and two serum albumins by spectroscopic approaches, J. Pharm. Anal. 3 (2013) 257–269.
[83] V.D. Suryawanshi, L.S. Walekar, A.H. Gore, P.V. Anbhule, G.B. Kolekar, Spectroscopic analysis on the binding interaction of biologically active pyrimidine derivative with bovine serum albumin, J. Pharm. Anal. 6 (2016) 56–63.
[84] M. Mąciazek-Jurczyk, J. Równicka Zubik, R. Dyja, A. Sułkowska, Comparative analysis of KP-HSA complex by spectroscopic methods, Acta Phys. Pol. A 123 (2013) 673–680.
[85] Y. Casamayou-Boucau, A.G. Ryder, Quantitative analysis of weakly bound insulin oligomers in solution using polarized multidimensional fluorescence spectroscopy, Anal. Chim. Acta 1138 (2020) 18–29.